Available on CMS information server

CMS NOTE 2006/138

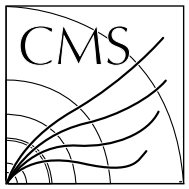

The Compact Muon Solenoid Experiment

CMS Note

Mailing address: CMS CERN, CH-1211 GENEVA 23, Switzerland

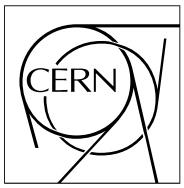

28 May 2007

Design, Performance, and Calibration of CMS Hadron-Barrel Calorimeter Wedges

CMS HCAL Collaboration

G. Baiatian, A. Sirunyan

Yerevan Physics Institute, Yerevan, Armenia

I. Emeliantchik, V. Massolov, N. Shumeiko, R. Stefanovich

NCPHEP, Minsk, Belarus

J. Damgov, L. Dimitrov, V. Genchev, S. Piperov, I. Vankov

Institute for Nuclear Research and Nuclear Energy, Bulgarian Academy of Science, Sofia, Bulgaria

L. Litov

Sofia University, Sofia, Bulgaria

G. Bencze, G. Vesztergombi, P. Zalan

KFKI-RMKI, Research Institute for Particle and Nuclear Physics, Budapest, Hungary

H. Bawa, S. Beri, V. Bhatnagar, M. Kaur, J. Kohli, A. Kumar, J. Singh

Panjab University, Chandigarh, 160 014, India

B. Acharya, Sud. Banerjee, Sun. Banerjee, S. Chendvankar, S. Dugad, S. Kalmani, S. Katta, K. Mazumdar, N. Mondal, P. Nagaraj, M. Patil, L. Reddy, B. Satyanarayana, K. Sudhakar, P. Verma

Tata Institute of Fundamental Research, Mumbai, India

S. Paktinat[1)]

Institute for Studies in Theoretical Physics and Mathematics, Tehran, Iran

I. Golutvin, V. Kalagin, I. Kosarev, G. Mescheryakov, S. Sergeyev, V. Smirnov, A. Volodko, A. Zarubin

JINR, Dubna, Russia

V. Gavrilov, Y. Gershtein[2)], V. Kaftanov[3)], I. Kisselevich, V. Kolossov, A. Krokhotin, S. Kuleshov,

[1)] Also at Sharif University of Technology, Tehran, Iran.

[2)] Now at Florida State University, Tallahassee, FL, USA.

D. Litvintsev[4], V. Stolin, A. Ulyanov

ITEP, Moscow, Russia

A. Demianov, A. Gribushin, O. Kodolova, S. Petrushanko, L. Sarycheva, I. Vardanyan, A. Yershov

Moscow State University, Moscow, Russia

V. Abramov, P. Goncharov, A. Khmelnikov, A. Korablev, Y. Korneev, A. Krinitsyn, V. Kryshkin, V. Lukanin, V. Pikalov, A. Ryazanov, V. Talov, L. Turchanovich, A. Volkov

IHEP, Protvino, Russia

T. Camporesi, T. de Visser, E. Vlassov[5]

CERN, Geneva, Switzerland

S. Aydin, I. Dumanoglu, E. Eskut, A. Kayis-Topaksu, A. Kuzucu-Polatoz, G. Onengut, N. Ozdes-Koca

Cukurova University, Adana, Turkey

K. Cankoçak[6], F. Ozok, M. Serin-Zeyrek, R. Sever, M. Zeyrek

Middle East Technical University, Ankara, Turkey

E. Gülmez, E. Isiksal[7], M. Kaya[8], S. Ozkorucuklu[9]

Bogazici University, Istanbul, Turkey

L. Levchuk, P. Sorokin

KIPT, Kharkov, Ukraine

B. Grinev, V. Lubinsky, V. Senchishin

Single Crystal Institute, Kharkov, Ukraine

E. W. Anderson, J. Hauptman

Iowa State University, Ames, IA, USA

J. Elias, D. Elvira, J. Freeman, D. Green, D. Lazic[10], S. Los, V. O'Dell, A. Ronzhin, I. Suzuki, R. Vidal, J. Whitmore

Fermi National Accelerator Laboratory, Batavia, IL, USA

G. Antchev, E. Hazen, C. Lawlor, E. Machado, C. Posch, J. Rohlf, S. X. Wu

Boston University, Boston, MA, USA

M. Adams, K. Burchesky, W. Qiang

University of Illinois at Chicago, Chicago, IL, USA

S. Abdullin, D. Baden, R. Bard, S. Eno, T. Grassi, C. Jarvis, R. Kellogg, S. Kunori, A. Skuja

University of Maryland, College Park, MD, USA

[3] deceased.

[4] Now at FNAL, Batavia, IL, USA.

[5] Also with ITEP, Moscow, Russia.

[6] At Mugla University, Mugla, Turkey.

[7] At Marmara University, Istanbul, Turkey.

[8] At Kafkas University, Kars, Turkey.

[9] At Süleyman Demirel University, Isparta, Turkey.

[10] Now at Boston University, Boston, MA, USA.

V. Podrasky, C. Sanzeni, D. Winn

Fairfield University, Fairfield, CT, USA

U. Akgun, S. Ayan, F. Duru, J. P. Merlo, A. Mestvirishvili, M. Miller, E. Norbeck, J. Olson, Y. Onel, I. Schmidt

University of Iowa, Iowa City, IA, USA

N. Akchurin, K. Carrell, K. Gümüş, R. Thomas

Texas Tech University, Lubbock, TX, USA

M. Baarmand, R. Ralich, I. Vodopiyanov

Florida Institute of Technology, Melbourne, FL, USA

P. Cushman, A. Heering[11)], B. Sherwood

University of Minnesota, Minneapolis, MN, USA

L. Cremaldi, J. Reidy, D. A. Sanders

University of Mississippi, Oxford, MS, USA

D. Karmgard, R. Ruchti

University of Notre Dame, Notre Dame, IN, USA

W. Fisher, J. Mans[12)], C. Tully

Princeton University, Princeton, NJ, USA

P. de Barbaro, A. Bodek, H. Budd, Y. Chung, T. Haelen, M. Imboden[13)]

University of Rochester, Rochester, NY, USA

S. Hagopian, V. Hagopian, K. Johnson

Florida State University, Tallahassee, FL, USA

V. Barnes, A. Laasanen, A. Pompos

Purdue University, West Lafayette, IN, USA

Abstract

Extensive measurements have been made with pions, electrons and muons on four production wedges of the Compact Muon Solenoid (CMS) hadron barrel (HB) calorimeter in the H2 beam line at CERN with particle momenta varying from 20 to 300 GeV/c. Data were taken both with and without a prototype electromagnetic lead tungstate crystal calorimeter (EB) in front of the hadron calorimeter. The time structure of the events was measured with the full chain of preproduction front-end electronics running at 34 MHz. Moving-wire radioactive source data were also collected for all scintillator layers in the HB. These measurements set the absolute calibration of the HB prior to first pp collisions to $\sim 4\%$.

[11)] Now at Boston University, Boston, MA, USA.

[12)] Now at University of Minnesota, Minneapolis, MN, USA.

[13)] Now at Boston University, Boston, MA, USA.

1 Introduction

The Compact Muon Solenoid (CMS) is a general purpose experiment designed to study pp collisions at the Large Hadron Collider (LHC) [1, 2]. The CMS experiment has a 4 T superconducting solenoidal magnet of length 13 m and inner diameter 5.9 m. The magnet determines many of the features of the CMS calorimeters because they are located inside it. The hadron calorimeter (HCAL) plays a fundamental role in most anticipated discoveries at the LHC [3]. The HCAL is used to measure the timing and energy of hadronic showers, needed for the generation of level-1 trigger primitives, the high level trigger, and offline reconstruction of jets and missing transverse energy [4, 5, 6]. Figure 1 illustrates the calorimeters in the CMS solenoidal magnet. The cylindrically symmetric hadron barrel (HB) calorimeter surrounds the lead tungstate ($PbWO_4$) electromagnetic calorimeter (EB), and it consists of alternating layers of brass and plastic scintillator plates. The HB design maximizes the number of interaction lengths inside the coil. This necessarily requires minimizing the amount of space devoted to the active medium. The scintillator tiles are read out with embedded wavelength shifting (WLS) fibers which achieves the required compact design. This technology was first developed at Protvino and by the UA1 collaboration and has been successfully used in an upgrade of the CDF endcap calorimeter [7, 8, 9]. Brass was chosen as the absorber material because it is non-magnetic. This design makes construction relatively simple, lends itself to projective tower geometry, and eliminates uninstrumented gaps.

The CMS hadronic calorimeter (HCAL) contains 9072 readout channels organized into four subsystems: barrel (HB, 2592 channels), endcap (HE, 2592 channels), outer (HO, 2160 channels) and forward (HF, 1728 channels). This paper addresses the design, performance, and calibration of the HB. The performance of the HE, HO, and HF were also extensively investigated and are reported elsewhere [10].

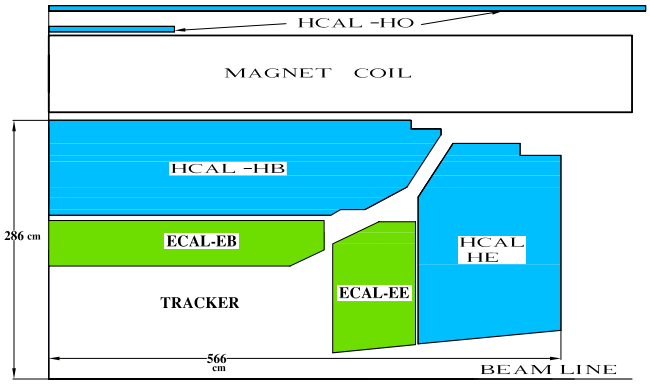

Figure 1: Location of the EB and the HB detectors (quarter slice) inside the CMS magnet coil.

While the beam tests of the HB prototype and bench tests of the calibration systems were reported previously [11, 12], this paper reports the first measurements of production modules with the complete electronics chain. As discussed in Section 9, one of the goals of this study was to relate the radioactive source measurements to beam measurements in order to calibrate the HB wedges which were not exposed to particle beams. After these measurements were performed, the HB wedges were assembled into the final barrel configuration.

This paper is organized as follows. The design details of the hadronic calorimeter are presented in Section 2. Topics related to electronics and data acquisition and the test beam setup are in Sections 3 and 4. Section 5 gives the HB performance in particle beams, while Section 6 describes the performance of the prototype electromagnetic module (EB). The results of the data analyses of the combined calorimeters are discussed in Section 7. In Section 8, a comparison of the combined results with Monte Carlo predictions is made. Following a summary of the radioactive source calibration in Section 9, we draw conclusions and summarize our work in Section 10.

2 HCAL Barrel Design

2.1 Absorber Geometry

The HB covers the pseudorapidity range $-1.3 < \eta < 1.3$ and consists of 36 identical azimuthal wedges ($\Delta\phi = 20°$) which form two half-barrels (HB+ and HB–). Each half-barrel is inserted from either end of the cryostat of the superconducting solenoid. Each wedge is further segmented into four azimuthal ($\Delta\phi = 5°$) sectors. The plates are bolted together in a staggered geometry resulting in a configuration that contains no projective passive material for the full radial extent of a wedge (see Figure 2). The innermost and outermost plates are made of stainless steel to provide structural strength. The scintillator is divided into 16 η sectors, resulting in a segmentation of $(\Delta\eta, \Delta\phi) = (0.087, 0.087)$. The wedges are bolted together and the gap between the wedges is less than 2 mm.

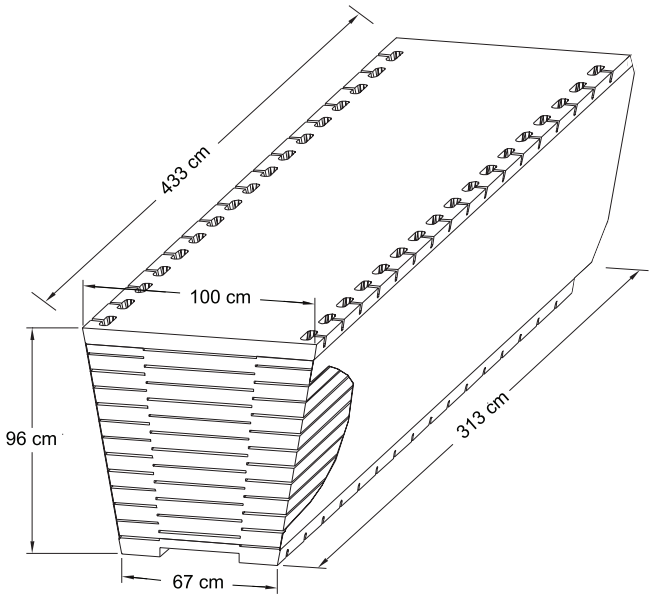

Figure 2: Isometric view of an HB wedge.

The absorber itself consists of a 40 mm thick front steel plate, followed first by eight 50.5 mm thick brass plates, and then six 56.5 mm thick brass plates, with a final 75 mm thick steel back plate. The total absorber thickness at 90° is 5.82 interaction lengths ($\lambda_{\rm I}$). The HB effective thickness increases with polar angle and is 10.6 $\lambda_{\rm I}$ at $|\eta| = 1.3$. The electromagnetic crystal calorimeter [13] in front of the HB adds $\sim 1.1\lambda_{\rm I}$.

The brass absorber is commonly known as C26000 (cartridge brass) and composed of 70% Cu and 30% Zn. The density is 8.83 g/cm^3. The radiation length is $X_0 = 1.49$ cm and the nuclear interaction length is $\lambda_{\rm I} = 16.42$ cm.

2.2 Scintillator

The CMS HCAL active elements consist of about 70,000 scintillator tiles. In order to limit the number of individual physical elements, the tiles of a given azimuthal section and depth layer are grouped into a single scintillator unit, referred to as a tray.

Figure 3 shows a typical tray. This design proved to be robust and practical. We tested each scintillator tray and the optical readout chain before installation into the absorber structure. The construction of the absorber structure and the scintillator assemblies were independent.

HB scintillator was 3.7-mm thick Kuraray SCSN81 plate. This scintillator choice was made because of its long-term stability and acceptable radiation hardness. The first layer of scintillator (Layer-0) is located in front of the steel support plate and is made of 9-mm thick Bicron BC408. The last scintillator layer (Layer-16) is 9-mm thick Kuraray SCSN81. These two layers are used to oversample early and late developing showers as is discussed below.

A tray is made of individual optically independent scintillators with white painted edges wrapped in Tyvek

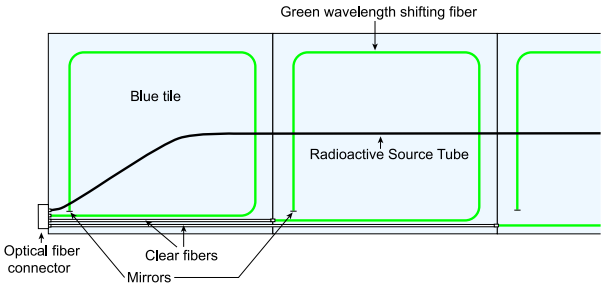

Figure 3: Schematic of a partial scintillator tray, showing WLS fibers, clear fibers, and the radioactive source tube locations.

1073D sheets. The scintillators are attached to a 0.5-mm thick plastic substrate with plastic rivets. Light from each tile is collected with a 0.94-mm diameter green double-clad wavelength-shifting fiber (Kuraray Y11) which is inserted in a ball-groove machined in the scintillator. The top of the tray is covered with a 2-mm thick white polystyrene sheet which carries the optical readout fibers. The wavelength shifting fibers are mirrored at the tip. The average reflectivity is $\sim 83\%$ with a spread of about 6.5% [14].

The wavelength shifting fibers are spliced to clear fibers to minimize optical attenuation in transporting the light from the scintillator plates to the photosensors located a few meters away. A fusion splicer was developed for this task and the light transmission across the splice is 92.6% with an *rms*of 1.8%. The clear fiber is terminated at a diamond-finished optical connector at the edge of the scintillator tray. An optical cable then further transports light to an optical unit which arranges the fibers into readout towers and guides the light to a hybrid photodiode (HPD) [15].

The completed tray is tested with a collimated ^{137}Cs source. This source illuminates a 4-cm diameter spot on the tray and is positioned with a computer controlled translation stage at selected locations on the tray. We determined the relative light yield of each tile and the uniformity of each tray. The response of individual tiles has an *rms*of 4.6%, while the transverse uniformity of a tile has a spread of 4.5%. These results imply that the tile uniformity contributes negligibly to the fractional energy resolution of the HCAL.

For calibration purposes, the top of each tray also houses a 1-mm diameter stainless steel tube, called *source tube*, that guides a ^{137}Cs (or ^{60}Co) source welded on the tip of a thin stainless steel wire across the center of each tile in a tray (Figure 3). During the assembly stage, the scintillator trays are tested by guiding the wire source through the source tubes. The *rms*of the ratio of the light yields with the collimated source to that of the wire source is 1.3%. This means the wire sources can be used to calibrate individual tiles to better than 2%.

2.3 Longitudinal Segmentation

The longitudinal segmentation of the HB is illustrated in Figure 4 (Table 1). Towers 1 through 14 all have a single longitudinal readout. Towers 15 and 16 are segmented in depth. The front segment of Tower 15 contains either 12 or 13 scintillator layers. The rear segment of Tower 15 has three scintillator layers. Tower 16 has five layers in the front segment and three in the rear. Tower 16 does not have a Layer-0 scintillator.

3 Electronics and Data Acquisition

Figure 5 shows an overview of the HCAL electronics and data acquisition system. All key elements were tested during these measurements.

Each wedge contains 72 channels of front-end electronics mounted on the detector periphery near Tower 14. These circuits are housed in an enclosure referred to as a readout box (RBX). Each of these RBXs is further divided into four readout modules (RM). A single RM contains an 19-channel HPD which registers signals from an independent $(\Delta\eta, \Delta\phi) = (0.0875, 0.0875)$ tower. The HPD is a planar structure consisting of a photocathode and a silicon diode separated by 3.5 mm away and all in vacuum. Photoelectrons are accelerated to ~ 8 kV kinetic energy and strike the diode causing ionization. Collection of the liberated

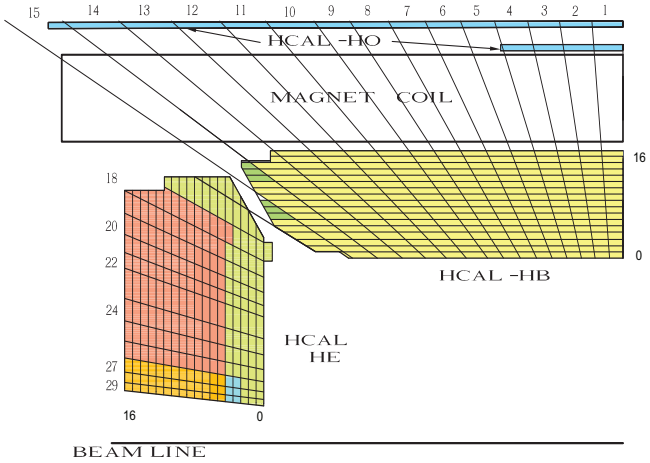

Figure 4: The HCAL tower segmentation for one-fourth of the HB, HO, and HE detectors is shown above. The numbers on top and on the left refer to the tower numbers. The numbers on the right and on the bottom (0-16) indicate the scintillator layers numbers inserted into slots in the absorber. The shading represents independent longitudinal readouts in the HB/HE overlap and the small angle regions.

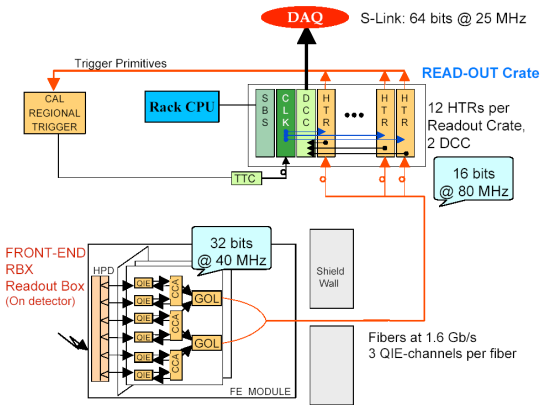

Figure 5: Overview of the HCAL data acquisition electronics. The data from the HPD are digitized in the QIE and driven off detector by the GOL (Gigabit Optical Link) driving optical fibers. Data are received in the HTR which creates trigger primitives while the data are sent through the DCC to the CMS data acquisition.

Table 1: The HB tower sizes and depths are summarized below. The thicknesses refer to the center of the tower. Note that Tower 16 overlaps with the HCAL endcap (HE) calorimeter. See also Figure 4.

Tower Number	$\eta_{\min} - \eta_{\max}$	Thickness ($\lambda_{\rm I}$)
1	0.000 - 0.087	5.39
2	0.087 - 0.174	5.43
3	0.174 - 0.261	5.51
4	0.261 - 0.348	5.63
5	0.348 - 0.435	5.80
6	0.435 - 0.522	6.01
7	0.522 - 0.609	6.26
8	0.609 - 0.696	6.57
9	0.696 - 0.783	6.92
10	0.783 - 0.870	7.32
11	0.870 - 0.957	7.79
12	0.957 - 1.044	8.30
13	1.044 - 1.131	8.89
14	1.131 - 1.218	9.54
15	1.218 - 1.305	10.3
16	1.305 - 1.392	overlaps HE

holes leads to a gain of about 1600. The gain is determined by the accelerating voltage and the value was chosen based on life-time tests. The diode consists of 19 electrically independent readouts. The HPD signals are fed into three 6-channel readout cards located inside the RM. These readout cards are based on a custom ASIC which performs charge integration and encoding (QIE) [16, 17]. The QIE is a non-linear multi-range ADC designed to provide approximately constant relative precision over a wide dynamic range. This is accomplished with a floating-point analog-to-digital conversion in which the bin width in each of four ranges is increased in proportion to the input amplitude. In addition, the QIE has four time-interleaved stages. The output of the QIE contains 2 bits of range (exponent) and 5 bits of mantissa.

3.1 Trigger and Readout Modules

The data are sent from the detector to HCAL trigger and readout modules (HTR) via gigabit optical links (GOL). Each link carries three channels of data. The HTR modules used for these measurements were 24 channel units in a 9U VME format. A total of six HTR modules were used to read out two HB wedges simultaneously (144 channels).

A block diagram of the HTR is shown in Figure 6. The HTR is equipped with optical receivers, timing and trigger (TTC) signal circuitry, serial low voltage digital signal (LVDS-Channel Link) outputs to the data concentrator card (DCC), and FPGA for trigger outputs. The optical inputs receive data from the front-end electronics, with one charge sample per bunch crossing.

The HTR includes two data pipe-lines. The trigger pipe-line assigns the front-end data to a particular LHC bunch crossing and sends them to the CMS trigger. The data acquisition pipe-line stacks the front-end data and sends it to the DCC which performs the data acquisition task. The raw input data stream is deserialized and synchronized to the local clock. A programmable delay of up to a few clock cycles is used to align data from different input fibers. The channels numbers carried on one fiber are demultiplexed. Each channel is then fed to a linearizing look-up table which converts the raw input data to a 16-bit linear energy value. Next, a finite-impulse response (FIR) filter is used to subtract the pedestal and assign all the energy to a single bunch crossing. The final synchronization and serial transmission is performed by a synchronization and link board (SLB).

3.2 Data Concentrator Card

The LVDS link receiver boards use Channel Link [18] technology from National Semiconductor. Each board contains three independent link receivers which can operate at 20–66 MHz (16-bit words). Buffering

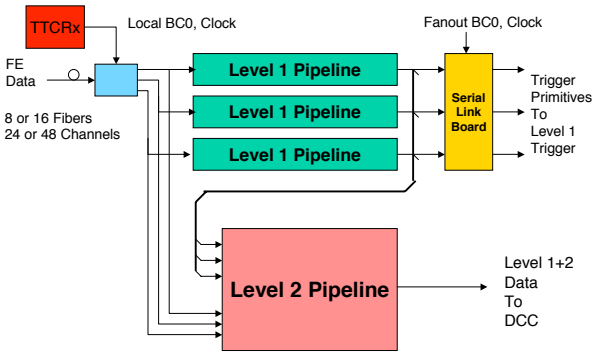

Figure 6: Block diagram of the HTR electronics. The data from the detector drives two pipelines; one to the CMS trigger and a second to the CMS data acquisition via DCC

for 128K 32-bit words is provided for each link with provision to discard data if buffer occupancy exceeds a programmable threshold. Event building, protocol checking, event number checking and bit error correction are performed independently for each link.

The DCC logic is designed to operate continuously at the full speed of the two input PCI busses, namely (33 MHz)×(32 bits)×(2). The event builder and output logic must thus run at an average rate of at least 66 MHz (32-bit words) or 264 MBytes/sec. The event builder output is sent in parallel to several destinations. The outputs are:

1. The data acquisition (DAQ) output: Every event is sent via SLINK-64 to the CMS DAQ. The contents of each event may be controlled by configuration registers.
2. The trigger data output: The trigger information sent to the CMS Level-1 trigger is also sent via SLINK-64 to a special trigger DAQ system for monitoring of the trigger performance.
3. The spy output: A selected subset of events is sent to a VME-accessible memory for monitoring and diagnostics.

Error detection and recovery are a primary consideration in a large synchronous system and the DCC contains logic dedicated to this purpose. Figure 7 shows the main DAQ data pipe-line and buffering. Hamming error correction is used for the LVDS links between the HTR and DCC. All single-bit errors are corrected and all double-bit errors are detected by this technique. Event synchronization is checked by means of an event number in the header and trailer of each event, which are checked against the TTC event number.

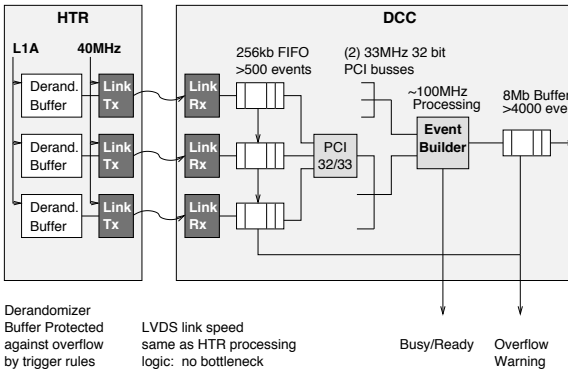

Figure 7: HCAL DAQ buffering schematic. The HTR sends the received data to the DCC. The DCC stores event fragments in FIFO buffers on the input and output.

4 Test Beam Setup

The data were recorded during 2002 at the CERN H2 test beam. A moving platform held two production HB wedges plus a prototype electromagnetic crystal calorimeter which was inserted in front of the HB for some of the measurements. The two-dimensional movement of the platform in ϕ and η directions allowed the beam to be directed onto any tower of the calorimeter. Four scintillation counters were located approximately three meters upstream of the calorimeters and a coincidence between a subset of these counters was used for the trigger.

4.1 ECAL Module

The electromagnetic calorimeter module used for the combined measurements consisted of 49 lead tungstate crystals arranged in a 7×7 array. The crystals are slightly tapered to form a projective geometry and are consistent with the CMS electromagnetic calorimeter design. Each crystal however was coupled to a single photo-multiplier tube (Hamamatsu R7524) through a plastic light guide located at the front of the crystal. The construction of this prototype roughly approximates the final configuration of the CMS EB in terms of spatial location of the crystals and approximate material between the EB and the HB. The PMT signals were digitized by CAEN V792 charge-to-digital converters (QDC). Five thermocouples were distributed inside the aluminum enclosure for temperature monitoring.

4.2 Data Sets

Data were taken with electron beam momenta of 20, 30, 50 and 100 GeV/c, pion beam momenta of 20, 30, 50, 100, and 300 GeV/c, and a muon beam of momentum 225 GeV/c. The momentum spread of the pion beam was established by collimators which were typically set better than $\Delta p/p = \pm 1\%$ and contributes negligibly to the calorimeter resolution.

Beams of muons, pions and electrons were directed into the centers of all towers, which included all four 5° sectors of the bottom wedge, but was limited to the bottom two 5° sectors of the top wedge for mechanical reasons. For both wedges, the scan covered the entire η range (16 sectors). These data were taken without the electromagnetic calorimeter module.

Additionally, several special runs were also taken with the moving radioactive wire source and with a LED pulser which illuminated the HPD. The measurements included a complete radioactive sourcing of all scintillator tiles (2092 tiles for each pair of wedges).

4.3 Determination of Layer-0 Weight

There is considerable inert material between the active elements of the EB and the HB. Therefore Layer-0 of the HB is used to sample early hadronic showers initiated either in the EB or in the inert material. The Layer-0 scintillator is thicker (9 mm) and brighter (BC408) than those in other layers in the HB. It produces more light and its sampling weight is controlled by an optical filter in the readout chain. We performed a series of measurements with filters in order to determined the proper sampling weight. The best energy resolution was obtained with a Layer-0 weight of $\alpha = 0.3$ as seen in Figure 8. Note that at $\alpha = 0.4$, a tail at large energy, which is particularly dangerous with steeply falling spectra is becoming evident. Conversely, the $\alpha = 0.2$ spectrum has a larger *rms*than that for $\alpha = 0.3$. These data were taken with an estimate of the material between the EB and the HB, and in the final production EB system, it was approximated as 8 cm of aluminum.

4.4 Noise Performance

The front-end electronics was operated at 33.79 MHz for all measurements reported in this paper. Figure 9 shows the noise distribution at the highest gain setting of the multi-range ADC, for a single QIE channel. The least count corresponds to 2080 electrons. The observed noise spread in the pedestal is less than 5000 electrons. As will be seen from the beam measurements, this corresponds to an energy of ~ 0.5 GeV.

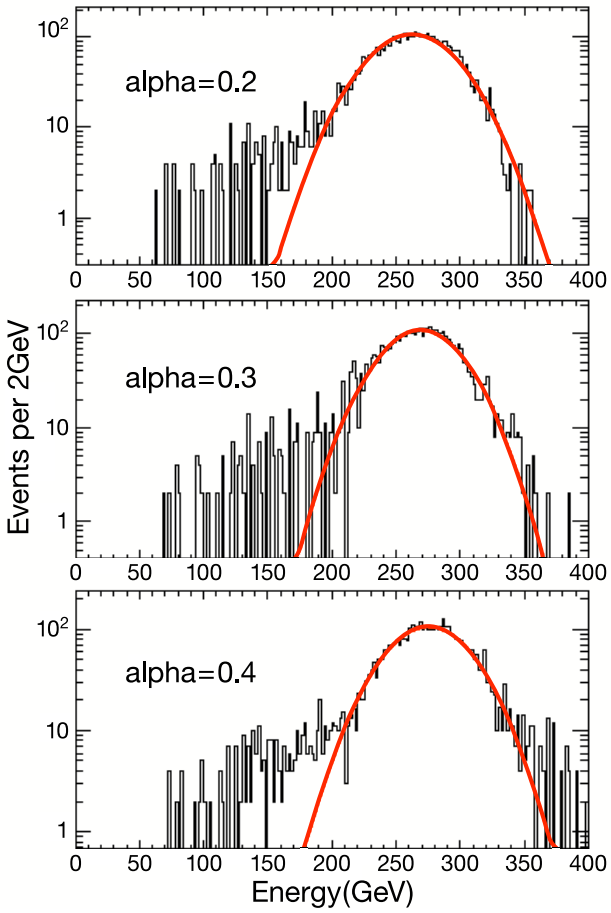

Figure 8: Single Gaussian fit to the signal distribution for 300 GeV/c pion beam with different weights applied to Layer-0. The plots correspond to a Layer-0 attenuation of 0.2, 0.3, and 0.4. Note the appearance of the high-side tail at $\alpha = 0.4$. A low-side tail at $\alpha = 0.2$ and the smallest Gaussian width shown at $\alpha = 0.3$.

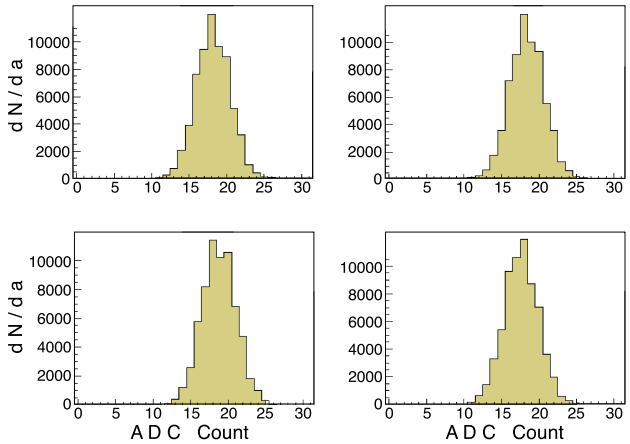

Figure 9: Measured pedestal distributions (dN/da) in units of raw ADC counts in the most sensitive QIE range for 4 capacitor banks of the QIE. The *rms* is 2.3 ADC counts, independent of which capacitor bank stores the charge.

4.5 Time Structure

The time structure of the HB pulse is dominated by the scintillator decay times. The front-end electronics, including the photo-detector is fast enough not to distort the pulse shape. The exact knowledge of the pulse shape is essential to correlate energy deposit with a particular LHC beam crossing. We made two different measurements of the time structure of the pulse of deposited energy. First, we investigated with a photomultiplier and commercial electronics; and second, we used the HPD and QIE electronics.

4.5.1 Measurements with a Photomultiplier Tube

We used a single 10-stage, 2-inch photo-multiplier tube (RCA 6342A) and the output was fed into a digital oscilloscope which recorded voltage in 0.4 ns bins. We recorded 300 GeV/c and 20 GeV/c pion and 100 GeV/c electron showers, as well as signals from high energy muons. Data from 300 GeV/c pions and 225 GeV/c muons are shown in Figures 10 and 11, respectively. In the case of muons, fluctuations in the number of photoelectrons lead to large event by event fluctuations.

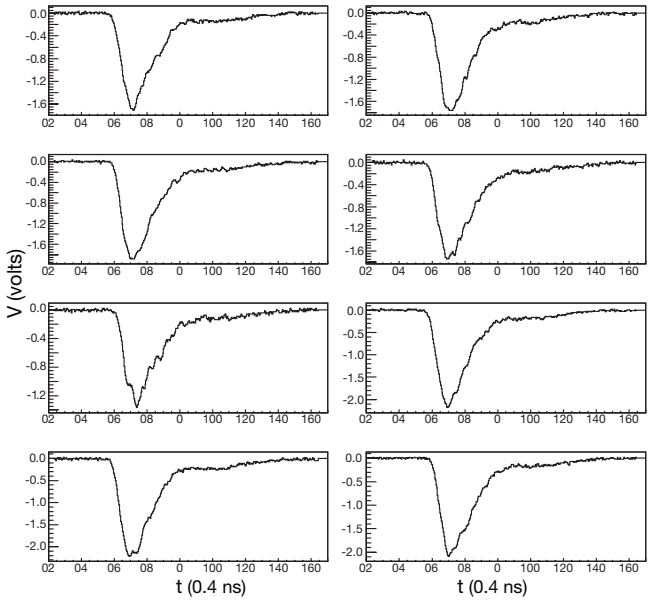

Figure 10: Calorimeter pulses for eight individual events, voltage *vs* time, observed with a photomultiplier for 300 GeV pion showers. The time scale is 0.4 ns per bin.

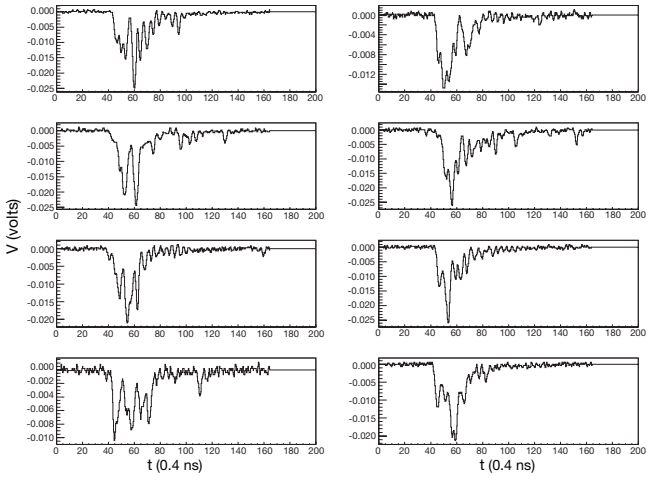

Figure 11: Calorimeter pulses for eight individual events, voltage *vs* time, observed with a photomultiplier for 225 GeV/c incident muons. The time scale is 0.4 ns per bin.

The pulse shape was observed to be very stable for showers. Figure 12 shows the fraction of energy observed in four consecutive time bins of width 29.6 ns. The pulse shape agrees very well with that of

measured by the HPD/QIE electronics.

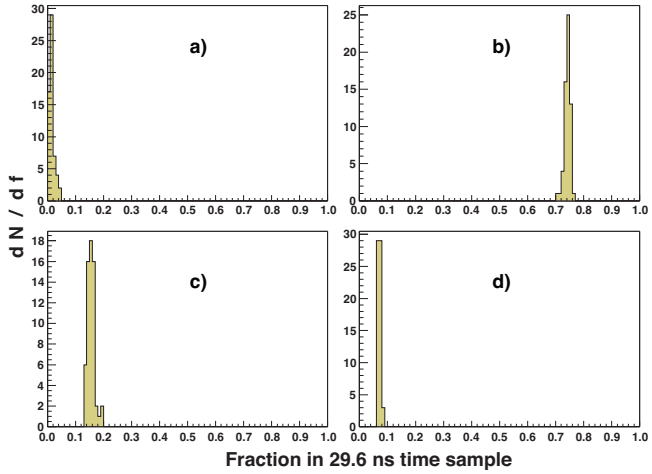

Figure 12: Fraction of energy (f) observed in 29.6 ns time samples for 200 GeV/c pion showers. a) first time sample, b) second time sample, c) third time sample, and d) fourth time sample.

4.5.2 HPD/QIE Measurements

Twenty time samples were recorded for each QIE channel. The timing was adjusted so that the event occurred near the middle of the time sequence (sample number 10) allowing us to record the noise performance well before and after the energy pulse. At a frequency of 33.79 MHz, each time sample corresponds to 29.6 ns (slightly longer than the 25 ns between LHC bunch crossings). Most of the signal is collected in two time samples. The reduced clock frequency used in these tests is the result of a design problem in the first procured QIE chips used at the time of data taking.

If we select the phase of the random test beam particles by requiring that 10-12% of the observed energy is in the 10th time sample, as shown in Figure 13, then all the events have the same temporal shape. We have the freedom to adjust this phase during the CMS running with programmable delays in the front-end electronics. Figure 14 shows the fraction of energy in two times samples (vertical scale) versus the fraction of energy observed in a single time sample (horizontal scale). The data points represent different choices of the phase. It is possible to have 75% of the energy in a single time sample and more than 90% of the energy in two time samples.

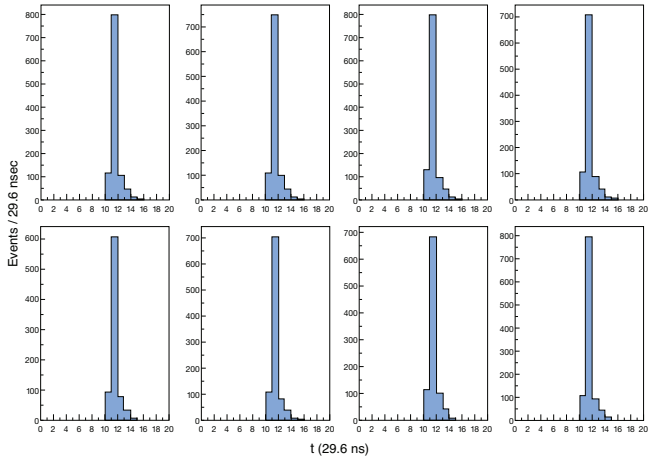

Figure 13: Time structure for eight events with 300 GeV/c incident pions in which the phase is selected by demanding that 10-12% of the observed energy is in time sample number 10.

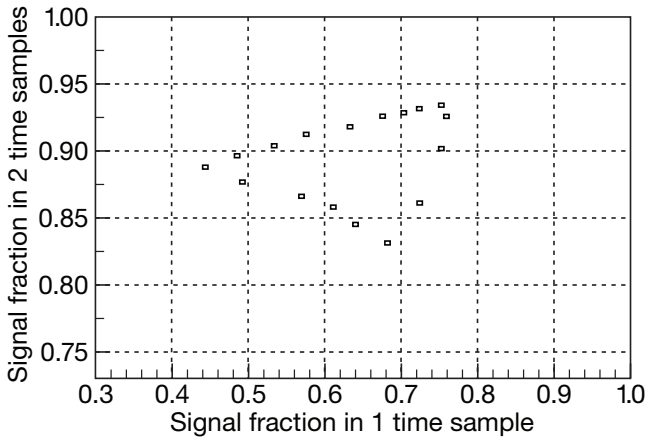

Figure 14: Fraction of signal observed in two time sample *vs* that observed in a single time sample. The zero point is suppressed for each axis.

5 The HB Response to Pions and Muons

The transverse containment of a hadronic shower in the HB is illustrated in Figure 15. With the 100 GeV/c pion beam centered on a tower, the fraction of energy observed in the single tower is on average 75%. If the energy in the neighboring eight towers is added, forming a 3×3 array, 93% of the pion energy is observed. The energy in a 5×5 array is 96%. The energy response for 100 GeV pions in a 5×5 array is shown in Figure 16. A Gaussian fit suggests that the energy resolution at this energy is about 10%.

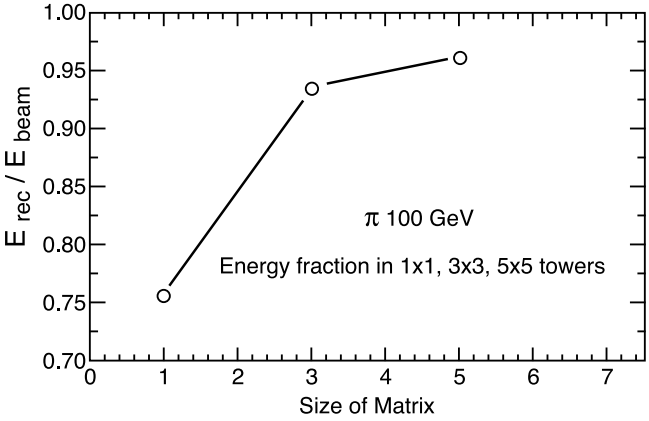

Figure 15: Average transverse containment of a 100 GeV/c pion shower, in terms of the energy fraction observed in a single (1×1) tower, a (3×3) array of 9 towers and a (5×5) array of 25 towers. The beam is centered on the array.

It is important to understand the response of the HB to muons not only for providing calibration redundant to the primary radioactive source method but also for particle identification purposes. A feature bit will be reported for use in higher level triggers, when a muon is identified by the HB. The signal, with 225 GeV/c incident muons, is about 2.5 GeV on average and clearly visible above the electronic noise (~ 0.5 GeV). Figure 17 shows the muon energy response from a single tower. A Landau fit to this distribution results in 1.64 GeV for the most probable and 2.5 GeV for the mean value.

6 The EB Response to Electrons

All 49 electromagnetic calorimeter crystals were calibrated with 100 GeV/c electrons. Note that a 5×5 crystal array in EB corresponds roughly to a single matching tower in the HB.

The linearity of response of the EB module was studied at electron beam energies of 20, 30, 50 and 100 GeV/c. The energy response is shown in Figure 18 at these four energies for 5×5 crystal array. Figure 19 displays the linearity of energy response as a function of beam energy derived from the Gaussian fits in Figure 18. The measured non-linearity between 20 and 100 GeV/c is $\sim$2%.

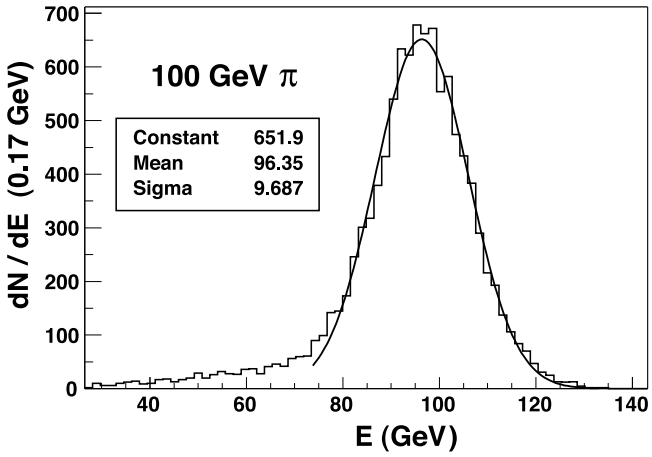

Figure 16: The energy distribution in the HB (5×5 towers) for 100 GeV/c pions. The solid line is a single Gaussian fit to the histogram data with best fit values for the Gaussian parameters shown in the figure legend.

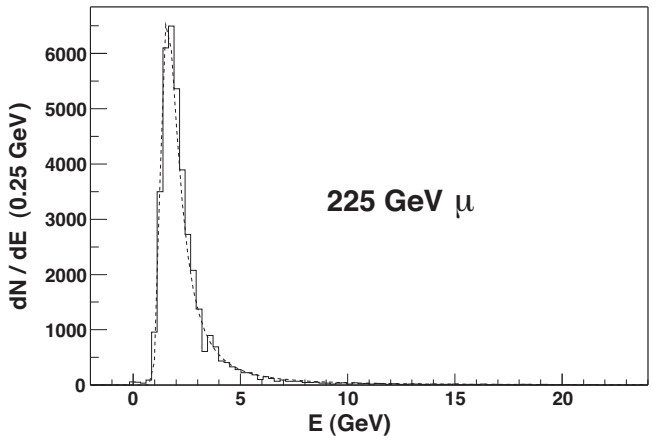

Figure 17: Observed energy distribution in the HB for 225 GeV/c incident muons. The most probable value for the energy deposited is 1.64 GeV while the mean is about 2.5 GeV. The dashed curve is the result of a fit to a Landau distribution.

The *rms*of the energy response at 100 GeV varied from 1.6 to 2.6 GeV depending on the data sets. Clearly the performance of this module is worse than the CMS ECAL [19]. However, the performance was satisfactory for the combined system investigations reported in this paper. The electronic noise for the sum of 3×3 crystals averages ∼0.7 GeV.

7 Performance of the Combined Calorimeters: EB+HB

7.1 Energy Resolution and Response

The performance characteristics of the HB and the EB module were studied with pion beams of varying momenta. These pion beams were contaminated with muons and electrons and the systematic errors caused by the cuts imposed to reduce these backgrounds are large at low momentum and are discussed below.

The absolute energy scale of the HB was defined using a beam of 50 GeV/c pions directed at the combined calorimeter systems. Only those pions which deposited less than 2 GeV in the EB were selected for the HB calibration. The calibration factor was extracted as the ratio between the pion beam momentum and the mean of the distribution of summed HB energy deposited in a 5×5 tower array centered on the beam position.

A series of cuts were developed to select pions in contaminated beams. Figure 20 shows the energy

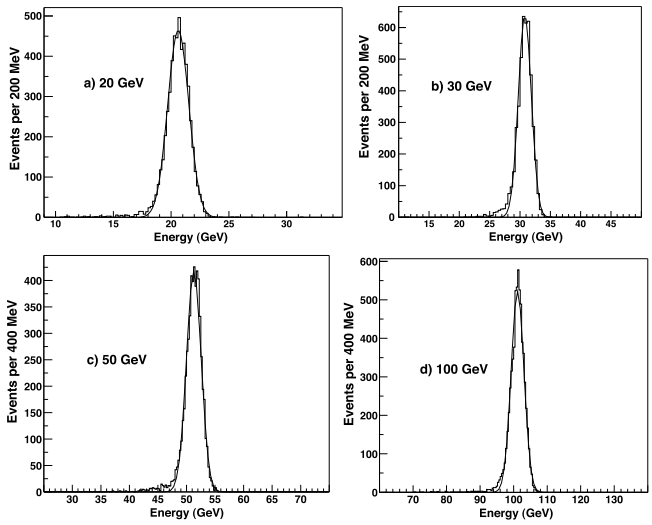

Figure 18: The single crystal EB response to incident electrons of energy a) 20, b) 30, c) 50, and d) 100 GeV/c. The smooth curves represent single Gaussian fits to the histogram data.

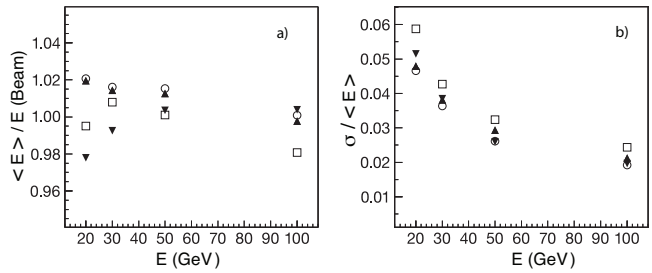

Figure 19: a) Mean energy divided by the beam energy *vs* the beam energy. b) The fitted Gaussian energy resolution *vs* the beam energy. The spread of the data points indicates the level of systematic error. The statistical errors are smaller than the size of the symbols. These points do not represent an optimized EB performance and the different symbols represent data taken at four different locations near the center of the 7×7 crystal array.

correlation between the HB and the EB for the case of 20 GeV/c pions. A cut $E_{\rm HB} > 6.5$ GeV, where $E_{\rm HB}$ is the HB energy, was applied in order to eliminate the events with abnormally small HB energy and also to remove electron contamination. An additional cut of $E_{\rm HB} > -0.83E_{\rm EB} + 5.2$ GeV, where $E_{\rm EB}$ is the energy measured by the EB, was made to reduce the muon background.

The energy response and resolution were determined from the Gaussian fits applied to the energy response distributions using the mean and the *rms*of the best fits.

These energy response and energy resolution measurements were corrected for the effect of the beam cuts, using a Monte Carlo simulation based on `GEANT4`. Beams of pions were generated and showered in the EB and the HB, and the resulting distributions were scaled up to match the measured mean energy. The quality cuts for background rejection were then applied and the correction factors were derived. The correction factors to the energy response and the resolution for 20 GeV/c (30 GeV/c) pions are 0.931 (0.987) and 1.056 (1.018), respectively. The corrections factors at higher energies are negligible.

There are three contributions to the quoted HB calibration error. One comes from the 2 GeV cut to the EB energy deposition by 50 GeV/c pions, and was estimated to be about 1% by varying this cut between 0 and 3 GeV. The second contribution comes from the background subtraction method applied to the 50 GeV/c calibration sample and it is estimated to be 0.5%. The third component is about 0.1% and comes from the statistical error on the mean of the 50 GeV/c distribution. Added in quadrature, the total calibration uncertainty is $\pm$1.3%. This error on the pion energy was propagated to the mean and width of the distributions by recalculating the total energy with the nominal, high, and low calibration factors.

Table 2 shows the results of the fits to the HB plus the EB energy response to pions. The fits are applied

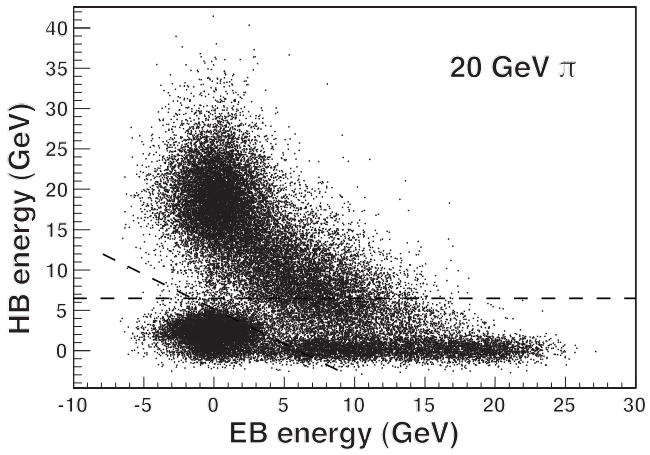

Figure 20: Energy observed in the HB *vs* the EB module for 20 GeV/c pions. The dashed lines show the cut limits which were imposed to remove muon and electron contamination in the beam.

to the raw data and no correction is made for the large e/h value of the electromagnetic calorimeter. The appropriate corrections will be made on data sets taken in 2006 when the beam cleanliness was greatly improved, when the beam momentum was extended down to 1 GeV/c and when a production CMS EB module became available for test. In this paper, we establish agreement with GEANT4 within the systematic errors and the available beam momentum range. The quoted energy resolutions are used to compare to the GEANT4 model and should not be taken as the ultimate performance of the combined CMS calorimeters. Figure 21 shows the energy resolution as a function of pion energy, and Figure 22 illustrates the non-linearity in response. The vertical bars are the statistical and systematic uncertainties added in quadrature. The comparison with GEANT4 is discussed in the next section.

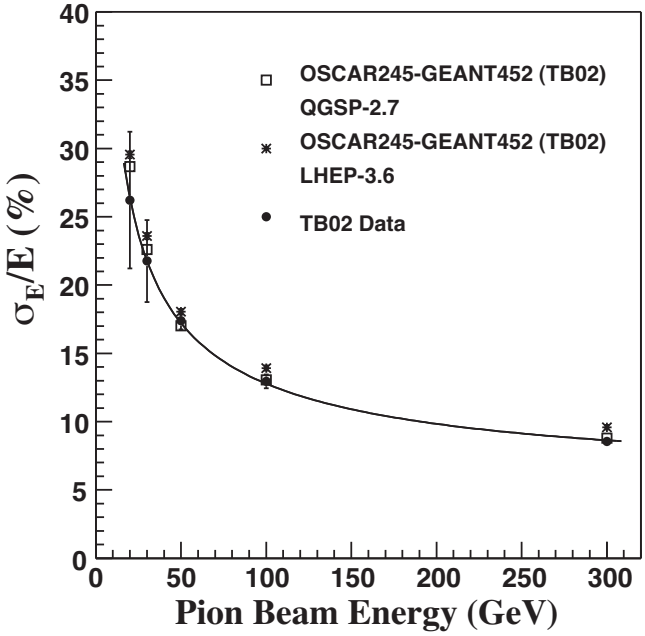

Figure 21: The measured energy resolution (solid circles) with fit (solid line) $(\sigma/E) = \frac{115.3\%}{\sqrt{E}} \oplus 5.5\%$ compared to two different tunes of GEANT4 (open squares and stars). The symbol $\oplus$ implies that two terms are added in quadrature.

8 Comparison with GEANT4

The CMS Collaboration developed the Object oriented Simulation for CMS Analysis and Reconstruction (OSCAR) framework [20], based on the GEANT4 tool kit, to describe the detector geometry and the passage of particles through the detector material. GEANT4 uses either parametric (LHEP) or microscopic

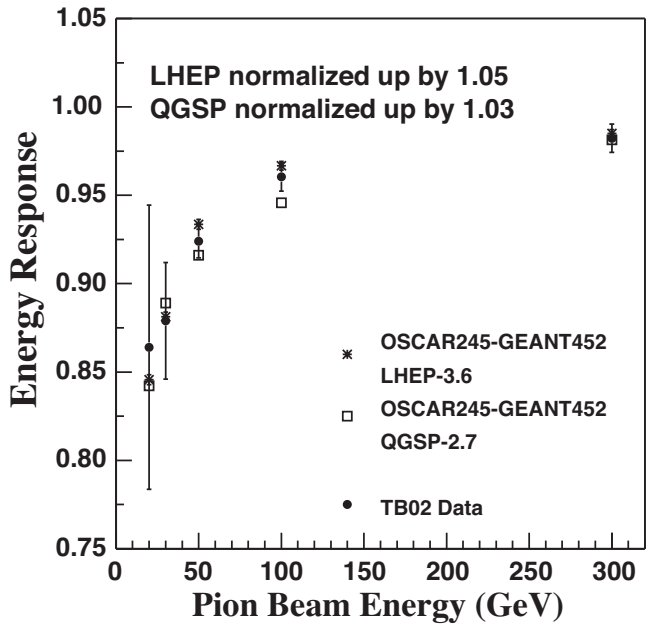

Figure 22: The measured energy response (solid circles) linearity compared to the GEANT4 simulations with different physics lists. The error bars indicate the statistical and systematic uncertainties added in quadrature.

Table 2: The energy resolutions and the associated errors ascribed to statistics, background and the calibration uncertainties for pions at five different beam momenta.

p_b (GeV/c)	$\overline{E}$ (GeV)	σ (GeV)	$\sigma/\overline{E}$ (%)	Stat. (%)	Bkg. (%)	Cal. (%)
20	18.2	4.5	26.5	0.15	5.0	0.1
30	26.9	5.8	21.6	0.12	3.0	0.2
50	46.2	8.0	17.3	0.10	0.6	0.2
100	96.0	12.4	12.9	0.07	0.4	0.3
300	295.0	25.2	8.5	0.05	0.0	0.3

(QGSP) physics models to simulate the particle showers arising from the interaction of particles with matter. For the studies presented in this paper, the software package OSCAR 2.4.5 is used, based on GEANT 4.5.2, with LHEP 3.6 and QGSP 2.7 physics lists or models.

A detailed comparison using GEANT4 was made for one tower location. The electronic noise was taken to be 520 MeV, in accordance with the pedestal measurement and the energy calibration scale. The secondary particle cuts were set to 1 mm for both electrons and positrons, and 10 mm for photons, except in the electromagnetic calorimeter where the photon cut was set to 1 mm.

The energy calibration of the EB and HB followed closely the same procedure used in the beam measurements. For 100 GeV/c electrons in the electromagnetic calorimeter, the two GEANT4 physics lists, LHEP-3.6 and QGSP-2.7, give energy resolutions in excellent agreement with each other.

For the EB, an additional scaling term was introduced so that the electron energy resolution simulated in the range 20-100 GeV/c agreed with the experimental values. The relative degradation in the energy resolution for pions when incorporating the extra smearing into the energy observed by the EB is 3% (1% absolute) at 20 GeV/c, and 0.6% (0.06% absolute) at 300 GeV/c.

The raw energy resolution of combined calorimeters is shown in Figure 21. The measurements are in good agreement with the simulation for the two physics lists tested. The LHEP-3.6 gives an energy resolution a few percent larger than the QGSP-2.7. The experimental data and the Monte Carlo predictions are more straightforward to compare in ratio as shown in Figure 23. The importance of the electronic noise contribution increases as the pion beam energy decreases. At 20 GeV/c, the resolution degrades by more

than 30% when a realistic electronic noise model is incorporated into the simulation.

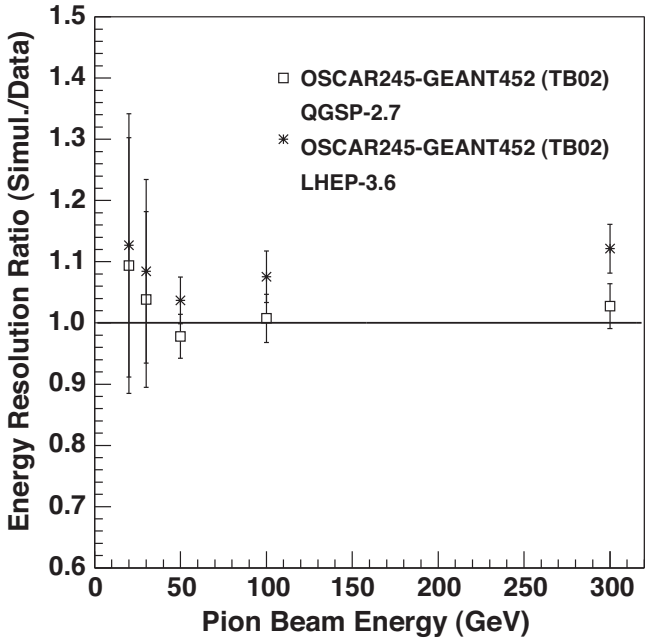

Figure 23: The energy resolution ratio of the different tunes of GEANT4 (open squares and asterisks) to the test beam data as a function of the pion beam energy. The solid line represents perfect energy independent agreement.

The simulation results on linearity of response are compared with the experimental data in Figure 22. For comparison, the simulated linearity plots were scaled up by 5% (LHEP) and 3% (QGSP) to approximately match the data at 300 GeV/c. There is good agreement between the experimental data and the simulation. While the LHEP-3.6 predicts a slightly faster growing response with energy compared to that measured, the one derived from the QGSP-2.7 increases more slowly. The electronic noise does not affect this measurement significantly. Figure 24 shows the ratio of energy response linearity between the simulation and the measurement.

9 Radioactive Source Calibration

The radioactive source calibration is performed for every scintillator tile. The ratio of the radioactive source signal to the energy response to the pions in the beam for each tower provides the initial calibration. This ratio depends on the type and activity of the source. The signals from 1745 tiles, corrected for the different fiber attenuation, are shown in Figure 25. The width of the distribution is 8% and it is consistent with the measurements of tile uniformity made during tray reconstruction. The difference in peak response taken while the wire radioactive source is extending versus retracting shows the reproducibility of the calibration signal is better than 1%.

The dependence of the ratio of radioactive signal to the electron signal on the tower number is shown in Figure 26. The same dependence for the ratio of radioactive signal to the muon signal is presented in Figure 27. The electron response agrees with the radioactive source measurements to an *rms*of 5%, while the muon data agrees to 3%. The greater spread in the electron data is attributed to the fact that the electron shower is concentrated in the first few scintillator layers, while the source measurement is averaged over all layers with equal weight as is the muon signal. Note that a single tile was manufactured with an 8% *rms*(see Figure 25). Thus electrons in the HB, which sample few tile layers have a 5% *rms*. The muon data are therefore better suited to establish the HB tower-to-tower relative calibration. The electron data, however, establish the absolute energy scale. Therefore, we have a cross check of the calibration initially established by pions.

The length of the optical fibers between the scintillators and the HPDs varies with η. Figure 28 shows the relative response to the radioactive source as a function of η. These data show that the light level at the HPD is about 30% lower for $\eta = 1$ towers when compared to $\eta = 14$ towers. The $\eta = 15$ and 16

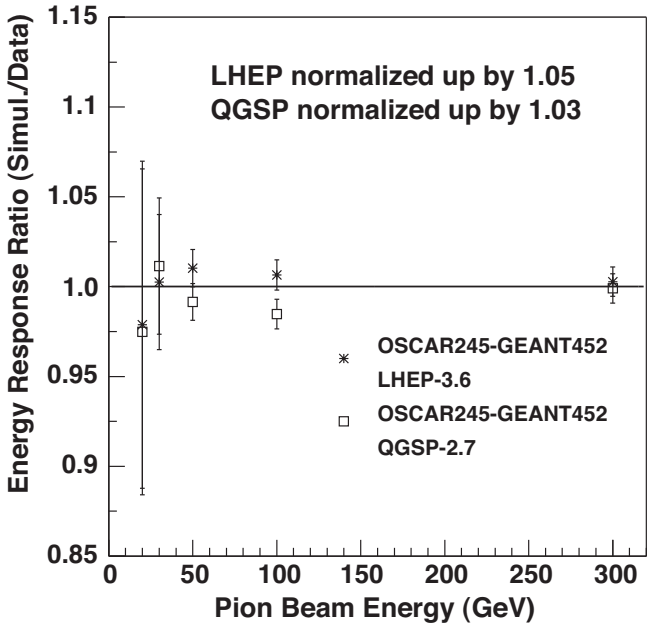

Figure 24: The energy linearity ratio of the different tunes of GEANT4 (open squares and asterisks) to the test beam data as a function of the pion beam energy. The solid line represents perfect energy independent agreement.

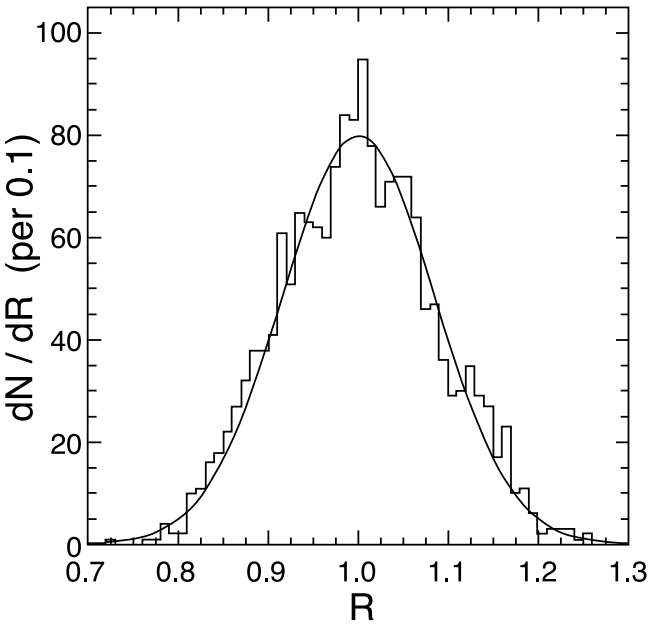

Figure 25: Distribution of scintillating tile response (R) to the source calibration normalized to the mean of the distribution. The line represents a single Gaussian fit to the data. The fitted *rms*spread of about 8% is consistent with the spread displayed by the collimated source measurements made during tile assembly.

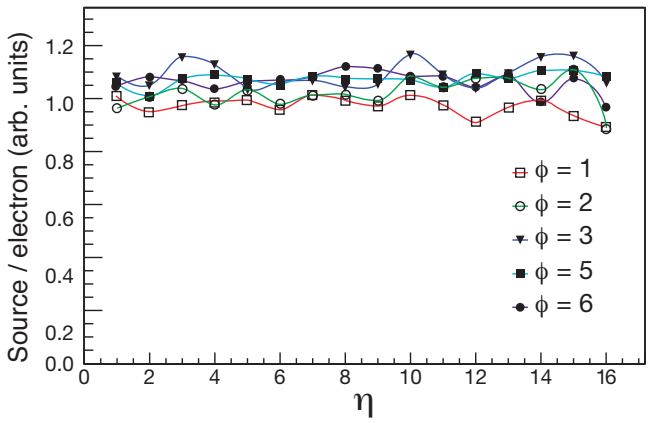

Figure 26: Ratio of the radioactive source signal (fit to peak value) to the 100 GeV/c incident electron signal in the HB *vs* η number of the tower for five different ϕ numbers (80 towers total).

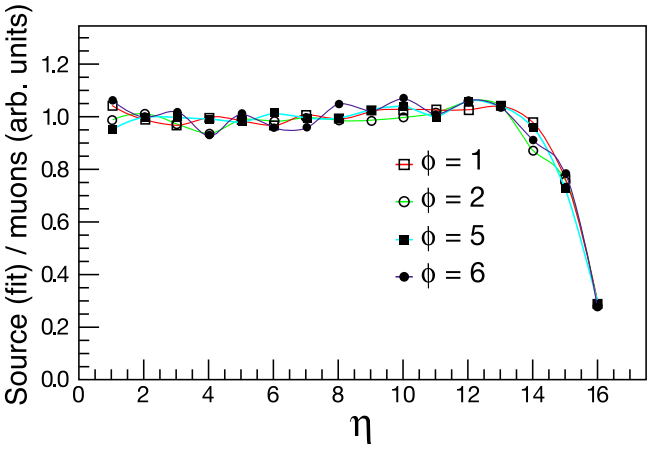

Figure 27: Ratio of the radioactive source signal to the HB signal due to a 225 GeV/c beam of incident muons *vs* η number for four different ϕ numbers (64 towers total). Towers with the number 15 and 16 have longitudinal segmentation which is not corrected for in this plot.

towers are not included in these measurements because they are segmented longitudinally.

A hadron shower is an intermediate case with large event by event fluctuations. A muon which samples 15 depth layers might be expected to have an *rms*of $8\%/\sqrt{16} = 2\%$. Indeed, the 8% manufacturing criterion was set so that tile uniformity would not be the major contributor to the constant term in energy resolution, which is dominated by non-compensation effects.

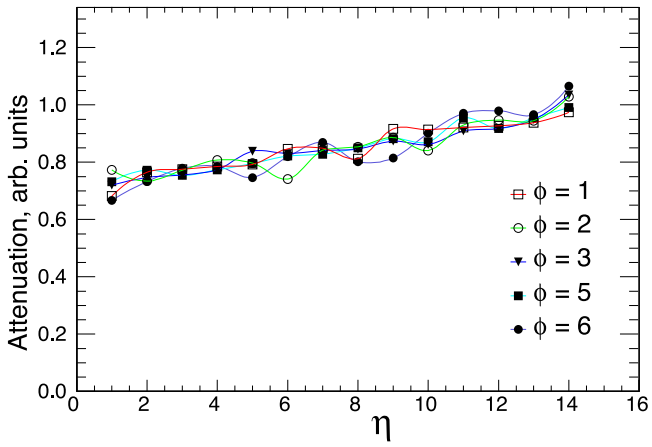

Figure 28: Measurement of the attenuation *vs* η number for five different ϕ numbers (80 towers total). The attenuation occurs in the propagation of the signals in fibers from the towers to the readout box which is located on the $\eta = 14$ end of the wedge.

10 Summary and Conclusions

The CMS Hadron Barrel (HB) calorimeter has been tested in a particle beam and the energy deposits have been compared to redundant techniques of initial calibration, radioactive sources and through-going muons. The data readout system used nearly final electronics operated at a slightly reduced clock frequency. Data were also taken in conjunction with an electromagnetic module (EB) which used similar crystals to CMS but completely different photodetectors and readout.

The noise performance of the HB readout, 0.5 GeV per time sample, was the same as measured in the laboratory. The time structure of the energy deposit pulse was consistent with the scintillator decay time and 75% of the pulse of the energy was deposited in a single 29.6 ns clock cycle. The energy deposit in the particle beam was compared to that deposited by a radioactive source and a through-going muon (2.5 GeV deposited). The quality of the comparison implies that the HB can be calibrated to about 4% prior to first data by transferring the beam calibration using the source data, and then cross checking using cosmic rays *in situ*.

The combined performance of EB+HB was measured and compared to the `GEANT4` Monte Carlo. The energy resolution has a 115% stochastic term and a 5.5% constant term over the beam momentum interval between 20 to 300 GeV/c. Agreement with `GEANT4` is adequate within the systematic errors. This performance, and the linearity of the response, was not optimized. That procedure awaits a clean low energy particle beam covering the low momentum interval of 2 to 10 GeV/c and the availability of an ECAL module which has the final CMS readout, both available in test beam data of 2006. The radioactive source system has proven to be a powerful tool for calibration of the HB to 4% accuracy, and an incisive commissioning tool in that each individual tile can be illuminated separately thus validating the complete readout chain.

Acknowledgements. This project was carried out with financial support from CERN, the U.S. Department of Energy (DoE), the U.S. National Science Foundation (NSF), RMKI-KFKI (Hungary, OTKA grant T 016823), the Scientific and Technical Research Council of Turkey (TÜBITAK), Turkish Atomic Energy Agency (TAEK), Bogazici University Research Fund (Grant no: 04B301), the Russian Ministry for Education and Science and the Russian State Committee for Atomic Energy.

References

[1] *CMS Technical Proposal*, CERN/LHCC 94-38, LHCC/P1 (December 1994).

[2] The LHC design report and current status is available at http://lhc-new-homepage.web.cern.ch/lhc-new-homepage/

[3] *The Hadron Calorimeter Technical Design Report*, CERN/LHCC 97-31 CMS TDR 2 (June 1997).

[4] *The TriDAS Project, Technical Design Report*, Volume 1: The Trigger Systems, CERN/LHCC 2000 - 38, CMS TDR 6.1, 599 pages, December 15, 2000.

[5] *The TriDAS Project, Technical Design Report*, Volume 2: Data Acquisition and High-Level Trigger, CERN/LHCC in press, 530 pages, December 2002.

[6] The HCAL/JetMET offline activities are described at http://www.uscms.org/scpac/JetMet/.

[7] V. I. Kryshkin and A. I. Ronzhin, Nucl. Instr. Meth. **A247** (1986) 583.

[8] M. G. Albrow *et al.*, Nucl. Instr. Meth. **A256** (1987) 23.

[9] G. W. Foster, J. Freeman, and R. Hagstrom, Nucl. Phys. **B23** (1991) 93; P. de Barbaro *et al*, Nucl. Instr. Meth. **A315** (1992) 317.

[10] G. Baiatian (CMS HCAL Collaboration), *Design, Performance, and Calibration of CMS Forward Calorimeter Wedges* CMS NOTE-2006/044;
Design, Performance, and Calibration of CMS Hadron-Barrel Calorimeter Wedges CMS NOTE-2006/138;
Synchronization and Timing in the CMS Hadron Calorimeter, CMS NOTE-2006/139;
Energy Response and Longitudinal Shower Profiles Measured in CMS HCAL and Comparison with `GEANT4`, CMS NOTE-2006/143.

[11] V. V. Abramov *et al* (CMS HCAL Collaboration), Nucl. Instr. and Meth. **A457** (2001) 75.

[12] E. Hazen *et al.*, Nucl. Instr. and Meth. **A511** (2003) 311.

[13] *The Electromagnetic Calorimeter Technical Design Report*, CERN/LHCC 97-33, CMS TDR 4 (Dec. 1997).

[14] E. Hernandez *et al* Radiation Phys. and Chem. Vol 41 No1/2 (1993) 409.

[15] P. Cushman, A. Heering, and A. Ronzhin, Nucl. Instr. and Meth. **A442** (2000) 289.

[16] T. Zimmerman and M. Sarraj, IEEE Trans. Nucl. Sci. NS-43 (1996) 1683.

[17] T. Zimmerman and J. R. Hoff, IEEE J. Solid-State Circuits 39 (2004) 895.

[18] The Channel Link is described in the National Semiconductor data sheet, *DS90CR285/DS90CR286, +3.3V Rising Edge Data Strobe LVDS 28-Bit Channel Link-66 MHz*, (November 2000).

[19] P. Adzic *et al*, Eur. Phys. J. C **44**, s02, 1-10 (2006).

[20] For CMS, the `GEANT4` simulation is incorporated into a package called Object oriented Simulation for CMS Analysis and Reconstruction (OSCAR), http://cmsdoc.cern.ch/oscar.